Microporous and Mesoporous Materials 175 (2013) 147–156

Contents lists available at SciVerse ScienceDirect

Microporous and Mesoporous Materials

journal homepage: www.elsevier.com/locate/micromeso

A study of the formation of microporous material SAPO-37

Lu Zhang [a], Donghan Chen [a], Heng-Yong Nie [b], Yining Huang [a,*]

[a] Department of Chemistry, The University of Western Ontario, London, Ontario, Canada N6A 5B7
[b] Surface Science Western, The University of Western Ontario, London, Ontario, Canada N6G 0J3

ARTICLE INFO

Article history:
Received 24 December 2012
Received in revised form 2 February 2013
Accepted 8 March 2013
Available online 29 March 2013

Keywords:
SAPO-37
Molecular sieve
Dry gel conversion
Hydrothermal synthesis
Crystallization

ABSTRACT

The crystallization of microporous material SAPO-37 was studied under hydrothermal synthesis (HTS) and dry gel conversion (DGC) conditions. The evolution of the intermediate phases as a function of crystallization time was followed by several techniques including PXRD, SEM, AFM, and solid-state NMR. For DGC, SAPO-37 crystallizes from a semi-crystalline layered precursor containing large pores and sodalite cages, whose structure is held by weak nonbonding interactions. Si atoms are only incorporated in the later stage of the crystallization via the formation of aluminosilicate species. Under HTS conditions, the crystallization pathway of SAPO-37 is somewhat similar to that for DGC. The AFM data suggest that the crystal growth mechanism is "birth and spread", and the final SAPO-37 crystals have rough (1 1 1) surfaces terminated by different structural building units. The findings of the present work provide new physical insights into the formation of SAPO-37.

1. Introduction

Since the first report by Lok et al. in 1984 [1], silicoaluminophosphate molecular sieves (SAPO-*n*) have received much attention due to that they have been widely used in industry for separation and catalysis. These microporous solids not only exhibit properties characteristic of zeolites and aluminophosphate ($AlPO_4$-*n*) based molecular sieves, but also present physicochemical traits unique to their chemical compositions [2,3].

SAPO-based molecular sieves consist of tetrahedral oxide (TO_4) frameworks (T = Si, P, and Al) and can be viewed as silicon atoms being incorporated into an $AlPO_4$-*n* framework [2]. Flanigen and co-workers [4] proposed three Si substitution mechanisms: (1) Si incorporated into an Al site (SM I), (2) Si incorporated into a P site (SM II), and (3) two Si atoms for an Al–P pair (SM III). Lok et al. [5] and Flanigen et al. [4] further suggested that silicon mainly substitutes via the SM II and SM III. This argument was confirmed later by lattice simulations [6], which showed that Si islands with only Si–O–Al and Si–O–Si bridges formed by a combination of SM II and III are energetically favorable and that at lower concentrations, the substituted Si is dispersed.

SAPO-37 has Faujasite framework (FAU topology, Scheme 1) [3,7–9], and attracted much attention due to its catalytic performances [10–12]. Like most molecular sieves, SAPO-37 is usually prepared by hydrothermal synthesis method (HTS) from an aqueous hydrogel prepared by mixing phosphoric acid, alumina, fumed silica, as well as structure-directing agents (SDAs). Several studies on the structure, synthesis conditions, and thermal stability of SAPO-37 were reported, but relatively few dealt with details of the crystallization process [3,7,13–23]. Thus, the formation of SAPO-37 is still not well understood at a molecular level.

A different synthetic approach, namely dry-gel conversion (DGC), was introduced years ago as an alternative method to HTS [24–29]. This method involves conversion of pre-dried gel powder to a crystalline microporous material at elevated temperature and autogenous pressure (for reaction vessel typically used for DGC, see Supporting Information, Scheme S1). Unlike hydrothermal synthesis, DGC has several advantages for examining crystallization owing to its simpler reaction system where all the reactive species are confined in the solid phase [30]. However, the lack of the apparent liquid phase may result in limited mass transport, and therefore lower crystal growth rates. As such, the intermediates may be captured under the favorable circumstances. Since the dry-gel powder contains about 40% water, it is widely recognized that the information obtained under DGC conditions does provide insight into crystallization under HTS conditions [30].

In this paper, we present our work on the formation of SAPO-37 under both HTS and DGC conditions using a mixture of tetramethylammonium (TMA) and tetrapropylammonium (TPA) hydroxides as the structure-directing agents (SDAs). Si incorporation was also studied. The local environments of P, Al, Si, and SDA molecules in various solid intermediate phases formed during the synthesis were probed by ^{31}P, ^{27}Al, ^{29}Si, and ^{13}C magic-angle spinning (MAS) NMR. The $^{27}Al\{^{31}P\}$ and $^{31}P\{^{27}Al\}$ rotational-echo double-resonance (REDOR) were also used to detect the Al–O–P connectivity in the gel wherever needed. The evolution of the long-range ordering within intermediates was monitored by powder X-ray

* Corresponding author. Tel.: +1 519 661 2111x86384.
E-mail address: yhuang@uwo.ca (Y. Huang).

1387-1811/$ - see front matter © 2013 Elsevier Inc. All rights reserved.
http://dx.doi.org/10.1016/j.micromeso.2013.03.026

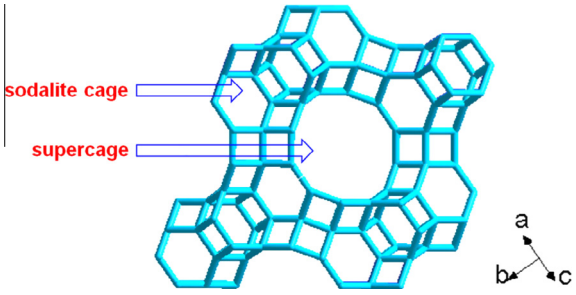

Scheme 1. Framework of SAPO-37.

diffraction (PXRD). Scanning electron microscopy (SEM) was utilized to observe the morphological changes. Further, the nucleation and crystal growth were examined by atomic force microscopy (AFM). The combination of these techniques provides new physical insights into the formation of SAPO-37.

2. Experimental

2.1. Sample preparation

The silicon, aluminum, and phosphorous sources were fumed silica Aerosil® 300 (Degussa), pseudo-boehmite (Catapal-B, Vista, ca. 65% Al_2O_3), and H_3PO_4 (EM Science, 85%). A mixture of tetramethylammonium hydroxide pentahydrate (TMAOH·$5H_2O$, Sigma–Aldirch) and tetrapropylammonium hydroxide (TPAOH, Alfa Aesar, 40% in water) was used as the SDAs. The initial gel composition (TPA_2O:TMA_2O:Al_2O_3:P_2O_5:SiO_2:H_2O) was 1.0:0.025:1.0:1.0:0.4:50 in a molar ratio [3]. The reaction mixture was prepared according to the work reported by Davis group [2]. Under HTS conditions, the mixture was put into several autoclaves and the crystallization was then carried out at 443 K. The autoclaves were quenched after specified lengths of time in cold water and the liquid phase in each autoclave was separated from the solid phase by centrifugation. The solid intermediates were carefully dried in air at room temperature and kept in tightly sealed glass vials once dried for further analysis. Under DGC conditions, the same reaction mixture was dried at 353 K with constant stirring until water was evaporated and solids formed. The solid dry gel was then ground into a fine powder and sealed in glass vials. It is hereafter referred to as the initial DGC dry gel. A series of intermediates were synthesized by placing 1.0 g of the initial DGC dry gel powder into small Teflon cups. Each cup was placed in a 23-mL Teflon-lined autoclave with 0.3 g distilled water at the bottom, and the autoclaves were heated in an oven at 473 K for different times. The reactions were quenched in cold water. For comparison, the solid sample from each cup was divided into two parts. One part was directly dried in air (unwashed sample) and the other part was first washed by stirring it with a small amount of water in a beaker and then dried in the same beaker in air without isolation from the liquid phase (washed sample). This ensured that no solid particles could be washed away. The solid gel samples were kept in tightly sealed glass vials.

2.2. Characterization

PXRD patterns were recorded on a Rigaku diffractometer using Co K_α radiation (λ = 1.7902 Å). A LEO 1540XB Field Emission Scanning Electron Microscope equipped with an energy-dispersive X-ray spectrometer was used for recording SEM images and elemental analysis. Representative samples were first coated with 3 nm osmium metal using a Filgen OPC-80T instrument.

All the NMR experiments were carried out on a Varian/Chemagnetics Infinityplus 400 WB spectrometer equipped with three rf channels operating at the field strength of 9.4 T. The Larmor frequencies of ^{1}H, ^{13}C, ^{31}P, ^{27}Al, and ^{29}Si were 399.5, 100.4, 161.7, 104.1, and 79.4 MHz, respectively. The magic angle was set using the ^{79}Br resonance of KBr. The chemical shifts of ^{13}C, ^{31}P, ^{27}Al, and ^{29}Si were referenced to adamantane, $NH_4H_2PO_4$, 1 M $Al(NO_3)_3$, and tetrakis(trimethylsilyl)-silane (TTMSS). Depending on the requirements of the individual experiment, we used three NMR probes (Varian/Chemagnetics 7.5 mm, 4.0 mm H/X/Y triple-tuned T3 MAS probe, and 5.0 mm H/F/X/Y triple-tuned MAS probe). The ^{13}C cross-polarization MAS (CP MAS) spectra were recorded by using the 5.0 mm probe with the Hartmann-Hahn conditions being optimized on adamantane. The ^{1}H 90° pulse length was 4 μs. A contact time of 2 ms was used and the pulse delay was 9 s. The proton-decoupling field was about 60 kHz. For ^{31}P MAS experiments, a 30° pulse was typically used and the recycle delay was 60 s. The ^{27}Al spectra were acquired using a very small pulse angle with a pulse delay of 1 s. For the ^{29}Si MAS experiments, a 45° pulse was used with a pulse delay of 60 s. For ^{1}H to ^{29}Si CP experiments, the ^{1}H 90° pulse length was 5 μs and the Hartmann–Hahn condition was determined using TTMSS. The rotational-echo double-resonance (REDOR) technique is a rotor-synchronized technique involving two separate experiments [31]. The first one is a normal spin–echo (S_0) on observed spin. The second (REDOR) experiment is also a spin–echo (S), but during the echo, a series of π-pulses are applied to the dephasing spin, which prevent the dipolar coupling from being refocused at the end of each rotor cycle. The REDOR difference spectrum ($\Delta S = S_0 - S$) indicates the dipolar interaction. ^{31}P{^{27}Al} and ^{27}Al{^{31}P} REDOR experiments were performed using the standard REDOR pulse sequence described in literature [31]. A 5.0 mm probe with a spinning speed of 8 kHz was used.

Surface structures of our SAPO-37 samples were studied with a Park Systems XE-100 AFM operated in the dynamic force mode using a cantilever with nominal spring constant of 40 N/m, resonant frequency of 300 kHz, and tip radius of 10 nm (NSC15, Mikro Masch). In this mode, the cantilever is vibrated at around the resonant frequency and its amplitude reduces when the tip is in proximity with the sample surface caused by the tip–sample interaction. Reduced amplitude is set as the feedback parameter (set point) so that the AFM system scans the surface contour of the sample with minimized error signals (the difference between the set point and the amplitude measured) by adjusting the distance between the tip and the sample surface. Mapping of this distance constructs topographic image for the surface morphology. On the other hand, mapping the error signal results in an image removing the height contribution and stressing only the shape of surface features. When the height range is large, surface features with small height differences are obscured in a topographic image. In this case, it is advantageous to use the error signal image to show the shapes of surface features, while using the topographic image to estimate the height distribution. The scan rate for obtaining images in an area of 45 × 45 μm^2 is 0.5 Hz and for images in an area of 10 × 10 μm^2 is 1 Hz. The experiment was conducted in air with a relative humidity of ~40%.

3. Results and discussion

3.1. HTS method

To follow the development of the long-range ordering of the intermediate phases, the PXRD patterns of gel samples were recorded as a function of crystallization time (Fig. 1). The pattern of the initial gel without heating and that of the gel samples heated below 16.5 h exhibit the patterns similar to that of the Al source, pseudo-boehmite (not shown), indicating that the solid phases

are X-ray amorphous and that most of the Al source has not yet reacted. Sharp diffraction peaks matching the pattern for SAPO-37 started to appear after heating the gel for 19 h and their intensities increase with the heating time. The PXRD patterns of the samples heated for 2 d or longer show only the reflections due to SAPO-37.

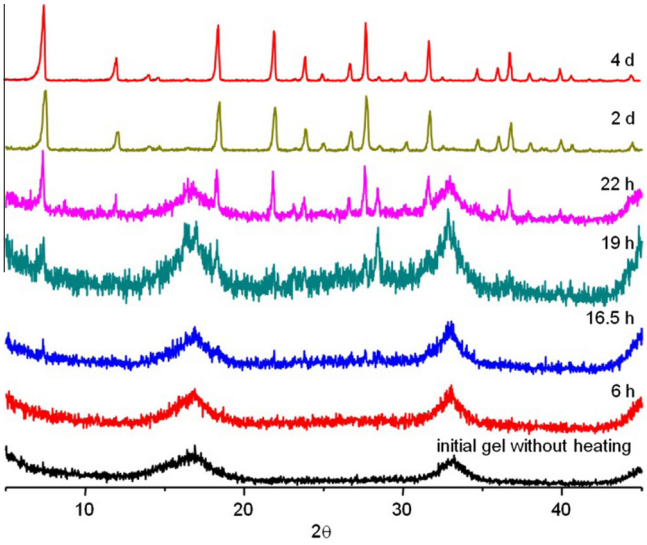

Fig. 1. Powder XRD patterns of the HTS samples.

Fig. 2 shows the SEM images of the selected HTS samples. Fig. 2A shows that for 22 h sample (Fig. 2A), the amorphous materials and SAPO-37 single crystals with typical octahedral morphology coexist, which is consistent with the corresponding PXRD pattern (Fig. 1) showing that the sample is a mixture of an amorphous phase and SAPO-37. Also visible are several spherical particles. The spherical particles are immediate precursor to SAPO-37, from which SAPO-37 crystallites develop. One such spherical particle labeled with a circle clearly exhibits an emerging (1 1 1) face. The 4 d sample is pure SAPO-37. Its SEM image (Fig. 2B) shows intergrown octahedra with (1 1 1) faces clearly visible.

The development of the local chemical environments of P and Al atoms in the gel phases as a function of crystallization time under HTS conditions is monitored by ^{31}P and ^{27}Al MAS NMR. In the ^{31}P MAS spectrum of the initial gel without heating (Fig. 3A), there is a very broad peak centered at around −12 ppm. The broadness of the peak indicates a wide distribution of P environment and the existence of many P containing species, which is consistent with the amorphous nature of the sample. These species are likely due to not fully condensed P sites with $P(OAl)_x(OH)_{4-x}$ or $(O)P(OAl)_x(OH)_{3-x}$ ($x = 1-3$) environments in the amorphous AlPO materials [32]. After heating the initial gel for 16.5 h, a new peak emerged at −26 ppm in the ^{31}P MAS spectrum. The chemical shift of this new peak is almost identical to the $P(OAl)_4$ environment in pure SAPO-37 [33]. It seems that although the sample is still X-ray

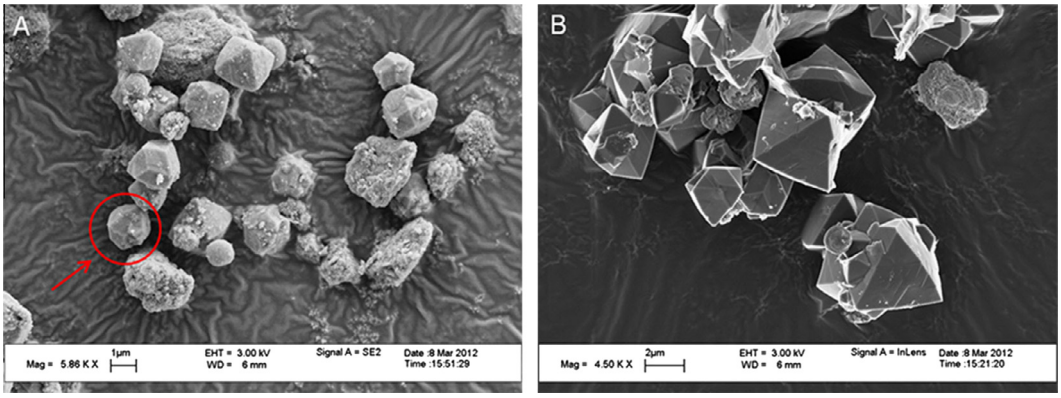

Fig. 2. SEM images of selected HTS samples. (A) 22 h and (B) 4 d.

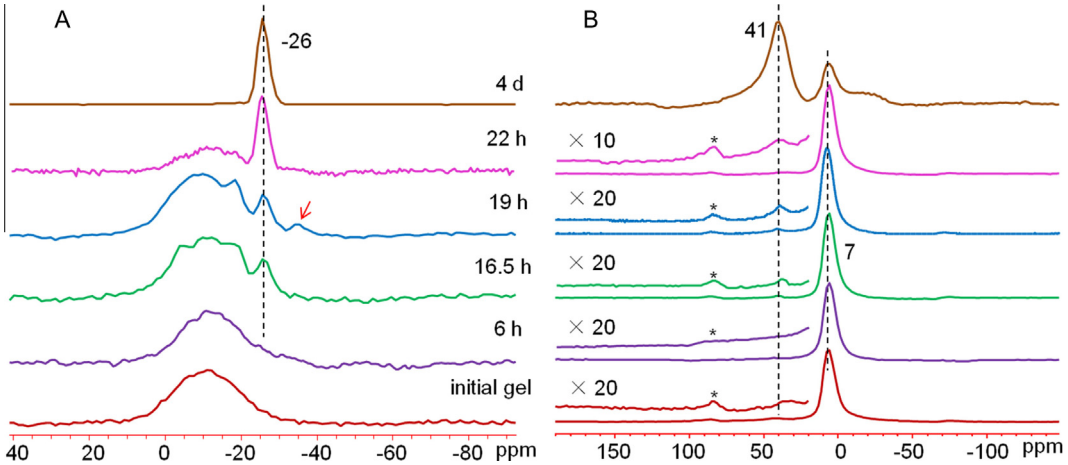

Fig. 3. (A) ^{31}P MAS and (B) ^{27}Al MAS spectra of selected HTS samples. Asterisks indicate spinning sidebands. The peak labeled with an arrow is due to $AlPO_4$-20 impurity.

amorphous, the local $P(OAl)_4$ environment similar to that of SAPO-37 has begun to form. The intensity of this peak increases with increasing the crystallization time at the expenses of the broad amorphous peak and eventually become a single sharp peak at −26 ppm, indicating that the amorphous materials have transformed into SAPO-37. A weak signal at −35 ppm in the 19 h sample is likely due to $AlPO_4$-20 impurity since it can also be synthesized by using a mixture of TPA^+ and TMA^+ as co-templates [34].

The ^{27}Al MAS spectrum of the initial gel without heating (Fig. 3B) shows a strong signal at 7 ppm and an extremely weak one at 41 ppm. The peak at 41 ppm falls within the reported range of 35–48 ppm for tetrahedral Al environment, $Al(OP)_4$, in the AlPO-based phase [34–37]. The resonance at 7 ppm results from the unreacted alumina (pseudo-boehmite) which also displays a peak at the same position [38]. The observed spectrum is consistent with those reported in the literature [22,23].

^{13}C CP MAS NMR technique is an effective tool to probe the tetraalkylammonium ions trapped in a microporous structure [39]. Fig. 4A shows the ^{13}C CP MAS NMR spectra of selected HTS samples. In the initial gel without heating, there are four signals. According to the literature, all of them belong to TPA^+ cations [2,17]. The signals at 60.9 and 15.6 ppm are assigned to the C_1- and C_2-methylene. The two peaks at 9.8 and 11.3 ppm originate from the methyl groups of the TPA^+ cations. The fact that the C_3-methyl group exhibits two signals in the initial gel indicates that the TPA^+ cations exist in different environments. A previous work found that the chemical shifts of TMA^+ cations adsorbed on the outer surface of SAPO framework and trapped inside sodalite (SOD) cage are 56.8 and 58.0 ppm, respectively [40]. Interestingly, none of these peaks was observed, suggesting that the TMA^+ cations are not present in the initial gel. Ito and co-workers [22,23] previously studied the crystallization of SAPO-37 by using ^{129}Xe NMR and reported that the initial gel and the sample heated for 5 h at 473 K already contain species having large cavities with 25 Å in diameter corresponding to the space of two supercages (the diameter of a supercage is 13 Å, see Scheme 2A for illustrations). They also pointed out that the connection between these species having large cavities is small and the arrangement of these species in solids is disordered. Since similar HTS synthesis conditions are used in the present case, the initial gel may also contain these large pore species. This is supported by the observation of a signal at 11.3 ppm, which is known to be the methyl of the TPA^+ trapped inside the supercage [2]. The 9.8 ppm peak is assigned to the TPA^+ adsorbed outside the large cavities [2]. The lack of ^{13}C signals due to TMA^+ indicates that no significant amount of sodalite cage has been developed.

Heating the initial gel for 16.5 h led to the appearance of a new peak as a weak shoulder at 58.5 ppm. As mentioned earlier, the chemical shift corresponds to the TMA^+ trapped inside the sodalite cage. It seems that the sodalite cages start to form in the gel, presumably associated with the large pore species (Scheme 2A) [2]. In the final product of SAPO-37, the ^{13}C peak assigned to the trapped TMA^+ becomes sharper, and the signals due to the TPA^+ are relatively broader, which suggests that the TMA^+ cations in the sodalite cages have higher mobility than the TPA^+ cations in supercages.

To examine the incorporation of the silicon atom into the framework under HTS conditions, ^{29}Si MAS NMR experiments were carried out (Fig. 5). Unlike other SAPOs [41–43] where the Si species in the initial gel and the gel obtained in the early stage of the crystallization are simply unreacted silica whose ^{29}Si spectra usually have a broad peak at −110 ppm, no meaningful ^{29}Si signal was observed in the solids heated for less than 19 h in this study. Since the silicon source used in this study is fumed silica that is in the form of very small particles, it seems that within short crystallization time, vast majority of fumed silica still remain suspended in the solution and were separated from the solids by centrifugation. In the 22 h sample, a weak signal at −90 ppm appears. The position of this peak is characteristic of isolated $Si(OAl)_4$ species in SAPOs [3,33,44], indicating the beginning of Si incorporation into the FAU framework. The intensity of the signal becomes sharper and stronger in the 2 d and 4 d samples, indicating that more Si atoms are incorporated into the SAPO-37 structure with increasing the heating time. There is also a broad shoulder at −94 ppm in these two samples, suggesting a small amount of $Si(OAl)_3(OSi)_1$ species [45].

EDX experiments were also carried out to semi-qualitatively estimate the substitution degree of Si atoms (Table 1). The Si content is about 14 mol.% in the final SAPO-37 sample, which is comparable to the upper threshold value (13%) of SM II mechanism in SAPO-37 framework [46]. The EDX data agree well with the corresponding ^{29}Si NMR spectrum discussed earlier. Both ^{29}Si NMR and EDX results suggest that under HTS conditions employed, Si is incorporated into the framework via both SM II and III mechanisms with SM II being the dominant one.

AFM has been used to image the detailed surface structures of zeolites and is able to provide key information on zeolitic crystal growth [47–51]. Several studies on the crystal growth of microporous materials with FAU structure such as zeolite Y and zincophos-

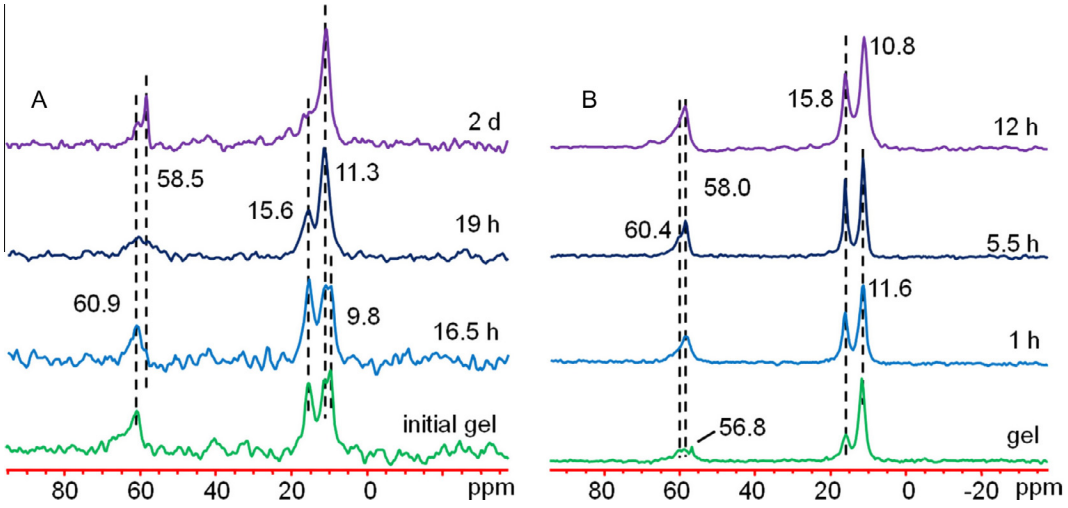

Fig. 4. ^{13}C CP MAS spectra of selected HTS samples (A) and DGC gel samples (B) with a contact time of 2 ms.

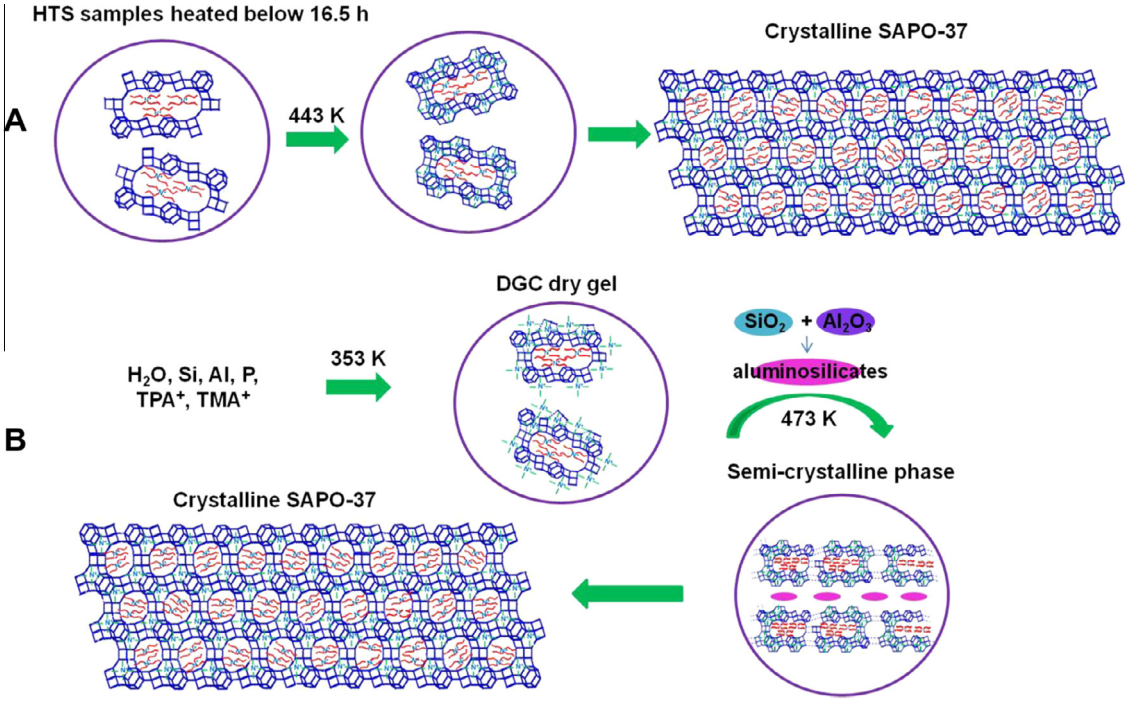

Scheme 2. Illustration of the formation of SAPO-37 under HTS (A) and DGC (B) conditions.

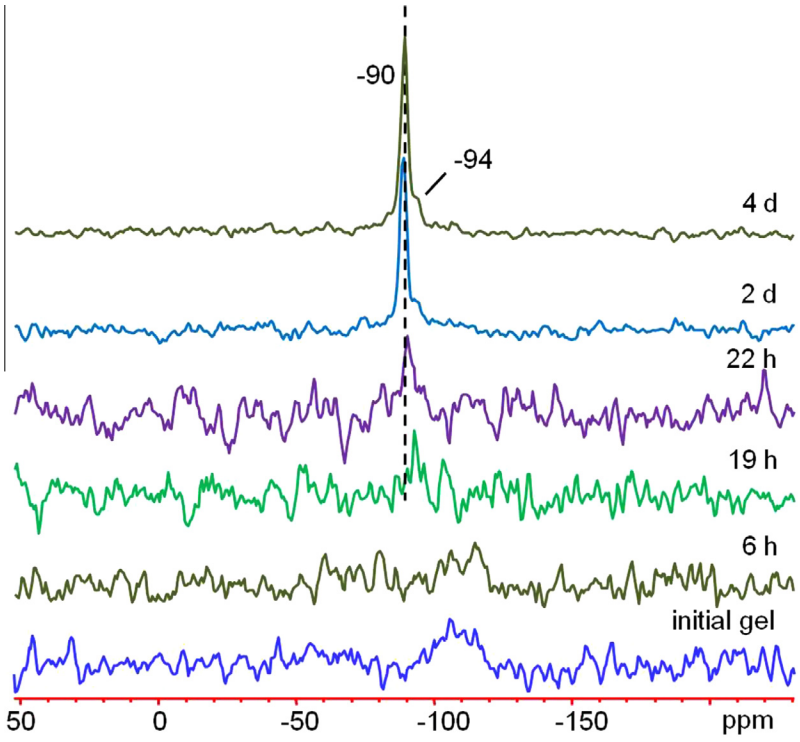

Fig. 5. ^{29}Si MAS spectra of selected HTS samples.

Table 1
Elemental compositions (molar basis) of selected gel samples.

Method	Sample	Si	Al	P	P/Al	(Si + P)/Al
HTS	4 d	0.14	0.48	0.37	0.77	1.08
DGC	5.5 h	0.09	0.48	0.43	0.90	1.08
	45 h	0.13	0.49	0.38	0.78	1.04

phate-faujasite (ZnPO-FAU) were reported [52–55]. In the present study, we utilize AFM to examine the surface feature of SAPO-37 crystals synthesized by HTS method. To date, this is the first study of nucleation and crystal growth of SAPO-37 by AFM.

Fig. 6A depicts an 8×8 μm^2 AFM image of one (1 1 1) face in a SAPO-37 crystal. Besides the intergrown structure in the face center, several terraces can be found on the surface. The magnified

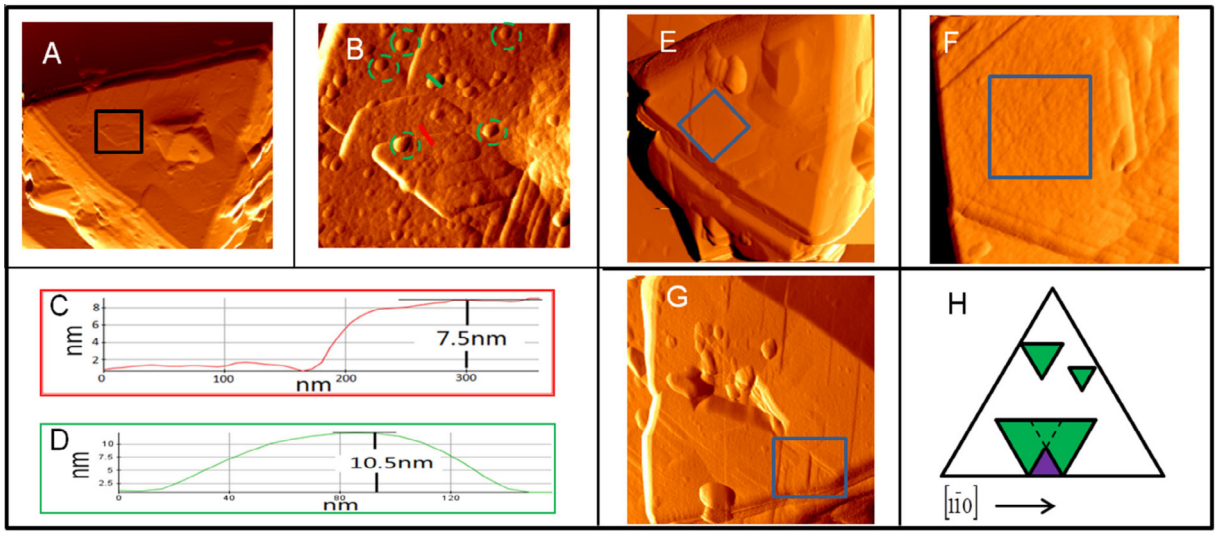

Fig. 6. AFM images of the (1 1 1) face of SAPO-37 crystals (4 d sample). (A) AFM image in an area of 8 × 8 μm^2; (B) enlarged view of an area of 2 × 2 μm^2 indicated in the black box in (A); (C) and (D) cross-sectional height profiles isolated from the AFM image along red and green lines shown in (B), showing the average height of surface steps and nuclei; (E) AFM image of the (1 1 1) face on another crystal in an area of 8 × 8 μm^2; (F) zoomed-in image of the blue square area in (E); (G) AFM image of a (1 1 1) face on a crystal in an area of 4 × 4 μm^2; (H) an illustrative scheme of triangle-shaped steps and dent pits on the (1 1 1) surface as indicated in the blue box in (G). For clarity, all AFM images in this figure are error signal images, while the height profiles are isolated from the corresponding topographic images (not shown). (For interpretation of the references to color in this figure legend, the reader is referred to the web version of this article.).

image (Fig. 6B) presents a rough (1 1 1) surface covered with these terraces as well as the nuclei on top of the terraces. This suggests that the rate of the terraces spreading to cover the whole (1 1 1) surface is slower than the nucleation rate. The nuclei grow all over the surface and on top of the terraces or other nuclei. They spread and coalesce with the terraces or nuclei underneath to cover the surface. This crystal growth mechanism is referred to as "birth and spread" [50]. Similar surface structures were reported before on the (1 1 1) face of the ZnPO-FAU crystals [56]. Section analysis (Fig. 6C and D) reveals that the terraces and nuclei in Fig. 6B have an average thickness of approximately 7.5 and 10.5 nm, which corresponds to the thickness of about 5 and 7 FAU layers (each FAU layer has a thickness of 1.43 nm) [54]. The thickness corresponding to one FAU layer was previously observed on the (1 1 1) surface of the zeolite Y and ZnPO-X crystals synthesized under HTS conditions [52,54,55]. Under the current synthesis conditions, both the heights of terraces and nuclei have much larger sizes than the reported value in zeolite materials [52,54,55].

Besides the above mentioned details on the SAPO-37 crystal surface, other crystal growth features were also observed. Fig. 6E shows the (1 1 1) face of a different crystal. Its magnified image (Fig. 6F) indicates that the steps on the (1 1 1) surface have triangular shapes rotated by 60° with respect to the crystal edge. Similar observations were reported for zeolite Y [54]. Fig. 6G shows a (1 1 1) face of a crystal with a large hollow pit in the center of the surface, indicating that SAPO-37 crystals have preference to start growing from the edges and then towards the center. A similar growth pattern was also observed for ZnPO-FAU [55]. Fig. 6G also displays a triangle-shaped dent near the edge of the crystal face. This type of triangular dent likely results from the coalescence of triangular shaped terraces as illustrated in Fig. 6H.

It should be pointed out the seemingly flat area on a given terrace such as the area in blue box in Fig. 6F is not atomically flat. For example, when zooming in on the terrace as indicated by the blue box area (Fig. 7A), a variation in height was observed. Interestingly, the heights are less than 1.43 nm (the height of one FAU layer). Two cross-sectional lines are drawn in the "flat" area inside box and their height profiles are shown in Fig. 7B and C. The height profiles along the two cross-sectional lines show the peaks with various heights such as 0.31 nm (corresponding to a 6-membered ring, 6R), 0.56 nm (corresponding to a double 6-membered ring, D6R), 0.87 nm (corresponding to an incomplete sodalite cage), and 1.28 nm (a height between that of a complete sodalite cage without D6R parallel to (1 1 1) plane (1.12 nm) and that of one FAU layer (1.43 nm)). See Fig. 7D for illustrations. Multiple steps with heights less than 1.43 nm were previously observed on the (1 1 1) face of zeolite Y crystals grown in aluminosilicate solutions [52]. By modeling the observed terminal structures, it was reported that complete D6Rs were the major surface structure. However, in the present study, the (1 1 1) surface growth is not terminated by the complete D6R. Instead, the (1 1 1) surfaces of SAPO-37 were terminated by different microstructures. It seems that instead of having uniform terminal structure on the surface, the (1 1 1) face of SAPO-37 crystals tends to be terminated by several building units such as 6Rs, D6Rs, as well as incomplete sodalite cages (Fig. 7D). It is worth noting that the intermediates and SAPO-37 crystals formed in the early stage of crystallization are not suitable for AFM study simply because their surfaces are covered with debris.

In summary, in the HTS study described earlier, the initial gel without heating appears to contain some species having large cavities with the TPA$^+$ cations trapped inside. These large cavities can evolve into supercages. Sodalite cages, on the other hand, form later, and they are templated by TMA$^+$ cations. These sodalite cages are likely to be associated with the species containing large pores. The amorphous material formed at this stage is a precursor and eventually evolves into FAU framework. Si incorporation occurs at later stage of the crystallization. Crystal growth on (1 1 1) face follows "birth and growth" mechanism. The surface structure is not terminated uniformly by one type of secondary building unit. The fact that the "incomplete soldiate cage" is found as terminal structure, suggesting that sodalite cage does not exist in the solution.

3.2. DGC method

The SAPO-37 formation was also studied by DGC method which simplifies the reaction system as all the reactive species present is confined in the solids. Fig. 8A shows the PXRD patterns of the un-

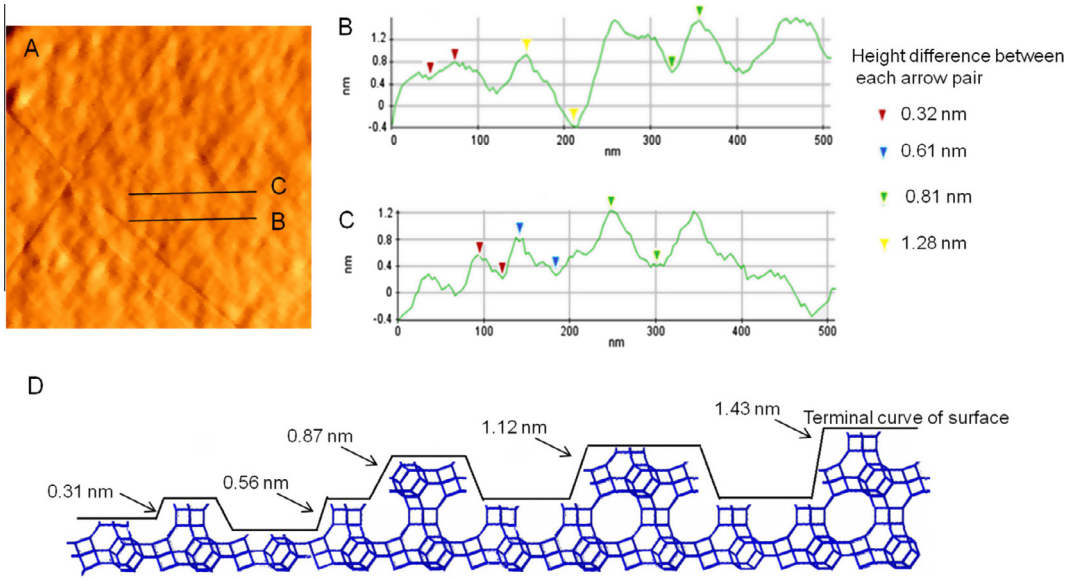

Fig. 7. (A) Topographic AFM image of the boxed area in Fig. 6F on a crystal in an area of 800 × 800 nm^2; (B and C) cross-sectional profiles along the lines in (A). Heights of ca. 1.28, 0.87, 0.56, and 0.31 nm are observed; (D) a model of the terminal structure of SAPO-37 along the lines in (A).

washed gel samples heated for different times under DGC conditions. The pattern of the initial dry gel dried at 353 K indicates that only amorphous materials exist. Upon heating the dry gel for 0.5 h, the PXRD pattern shows the appearance of a new broad peak with a very low 2θ value (labeled with an arrow). This peak becomes much strong after 1 h heating, implying that the majority of the amorphous materials transformed into a semi-crystalline layered phase. After washing with distilled water, the strong low-angle peak in 1 h sample became weaker and broader (Fig. 8B), demonstrating that part of the semi-crystalline phase transformed back to amorphous materials after washing. This indicates that the semi-crystalline phase is held by weak nonbonding forces such as van der Waals and/or weak hydrogen bonding; similar situation is also found in the crystallization of SAPO-34 and $AlPO_4$-based molecular sieves under DGC conditions [57–60]. After 5.5 h, the intensity of the strong low-angle peak due to the semi-crystalline phase began to decrease. The characteristic reflections due to SAPO-37 started to appear concomitantly, indicating the transformation of the semi-crystalline phase into the FAU framework. Heating the gel for 12 h results in the complete disappearance of the low-angle peak and the PXRD pattern indicates pure SAPO-37 with high crystallinity [3]. Further heating leads to the appearance of a small amount of impurity as shown in the PXRD pattern of the 45 h sample.

The SEM images of the selected DGC samples are shown in Supplementary Fig. S1. The picture of 5.5 h sample shows a large number of aggregated small octahedral crystals. The micrograph of 45 h shown in Fig. S1B is analogous to that of 5.5 h sample except that

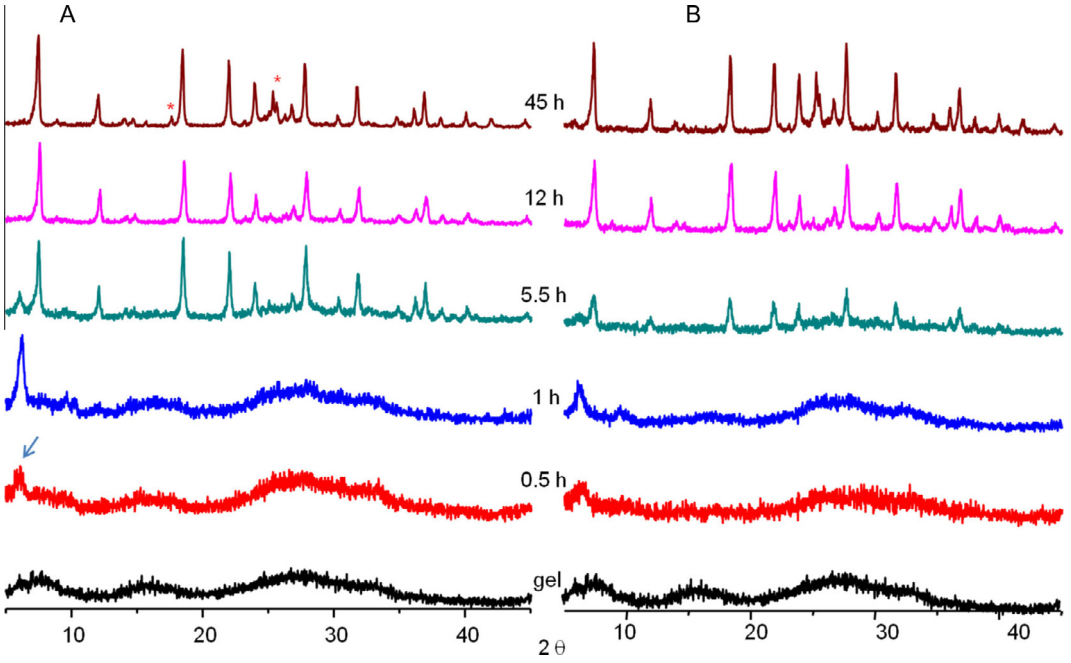

Fig. 8. (A) Unwashed and (B) washed powder XRD patterns of DGC gel samples. * indicates impurities.

the crystal sizes are slightly larger (0.2–0.3 μm). Due to the small crystal size, AFM characterization cannot be conducted on SAPO-37 crystals synthesized under DGC conditions.

The ^{31}P MAS spectrum (Fig. 9A) of the initial DGC dry gel shows a peak at −20 ppm and a broad hump on its high-frequency side. The presence of the broad hump is consistent with the amorphous nature of the initial dry gel. The ^{27}Al MAS spectrum of the initial gel (Fig. 9B) contains a relatively narrow peak at 41 ppm and a broad resonance at 6 ppm. To further understand the nature of the initial dry gel without heating, ^{27}Al{^{31}P} and ^{31}P{^{27}Al} REDOR experiments were carried out to establish the connectivity between P and Al atoms in the dry gel. The ^{27}Al{^{31}P} REDOR difference (ΔS) spectrum is shown in Fig. S2A. As mentioned earlier, REDOR technique is based on heteronuclear dipolar coupling. In the ^{27}Al{^{31}P} REDOR difference (ΔS) spectrum, only Al with P in its proximity will be observed. The fact that Fig. S3A only contains the peak at 41 ppm confirms that the tetrahedral Al is indeed in the AlPO-based material. The peak at 6 ppm did not appear in the ΔS spectrum, indicating unambiguously that this peak is due to unreacted alumina. ^{31}P{^{27}Al} REDOR difference spectrum (Fig. S2B) shows that the P site at −20 ppm is connected to the tetrahedral Al at 41 ppm and vast majority of the high-frequency signals in the ^{31}P MAS spectra are from phosphate species (presumably amine phosphates) without Al nearby. It seems that the initial dry gel contains unreacted alumina and amine phosphates as well as AlPO-based materials.

With increasing heating time, the 6 ppm peak in ^{27}Al MAS spectra and broad high-frequency signals in ^{31}P MAS spectra become weaker, implying that they further react with each other to form AlPO-based layered semi-crystalline intermediate. After heating the dry gel for 1 h, the very broad high-frequency signals in the ^{31}P MAS spectrum of the initial dry gel has almost diminished and the peak at −20 ppm is now the strongest peak (Fig. 9A). In the corresponding ^{27}Al MAS spectrum (Fig. 9B), the intensity of the resonance at 41 ppm due to the tetrahedral Al site in the AlPO phase is increased significantly at the expense of the intensity of the peak at 6 ppm. The changes in the ^{31}P and ^{27}Al MAS spectra coincide with the observed changes in the PXRD pattern of this sample, suggesting that the phosphates and alumina further react to form AlPO-based layered semi-crystalline intermediate. Upon heating the dry gel for 5.5 h, a new ^{31}P resonance at around −26 ppm started appearing with the peak at −20 ppm decreasing in its intensity. The formation of the −26 ppm peak suggests the development of a new phase in the gel sample. This agrees very well with the corresponding PXRD pattern (Fig. 8), which shows the appearance of the characteristic peaks due to SAPO-37 phase. The ^{31}P MAS and ^{27}Al MAS spectra of the 45 h sample (Fig. 9) only exhibit resonances characteristic of SAPO-37, confirming that the semi-crystalline phase transformed into SAPO-37 phase.

The ^{13}C CP MAS NMR spectra of selected DGC gel samples are shown in Fig. 4B. For the DGC dry gel, the peaks 58.0 and 56.8 ppm are from methyl groups of TMA$^+$. As mentioned before, these two peaks correspond to the TMA$^+$ cations trapped inside the sodalite cage (58.0 ppm) and adsorbed outside the surface of the solids (56.8 ppm). Seeing these peaks suggests that in the DGC dry gel, sodalite cage or quasi-sodalite cage already exists. The initial DGC dry gel was prepared by drying a solution containing all the reactive species at 353 K. It appears that under these conditions, quasi-sodalite cage forms around TMA$^+$. As discussed earlier, the signals at 60.4, 15.8 and 11.6 ppm are due to the C_1- and C_2-methylene as well as C_3-methyl groups of TPA$^+$, respectively. Observing the 11.6 ppm methyl peak from TPA$^+$ suggests that similar to the gel phase obtained under HTS conditions, the initial dry gel also contains the AlPO species having large cavities with trapped TPA$^+$.

Upon heating the dry gel for 1 h, the peak assigned to the adsorbed TMA$^+$ disappeared and only the signal due to the trapped TMA$^+$ is present, indicating that the TMA$^+$ ions initially adsorbed on the outer surface further direct the formation of the sodalite cage. Since the corresponding PXRD pattern and ^{31}P MAS spectrum show unambiguously that the sample only contains semi-crystalline layered phase and that SAPO-37 has not formed at this point, the ^{13}C NMR data suggest that the semi-crystalline layered intermediate contains the quasi-sodalite cage.

^{29}Si MAS NMR spectra (Fig. 10A) were acquired to follow the incorporation of Si into the framework under DGC conditions and ^{1}H to ^{29}Si CP technique was also utilized to select the Si species with protons in its close proximity (Fig. 10B). The ^{29}Si MAS spectra of the DGC dry gel and the gel sample heated for 1 h show a broad peak centered at around −112 and −108 ppm, respectively. These

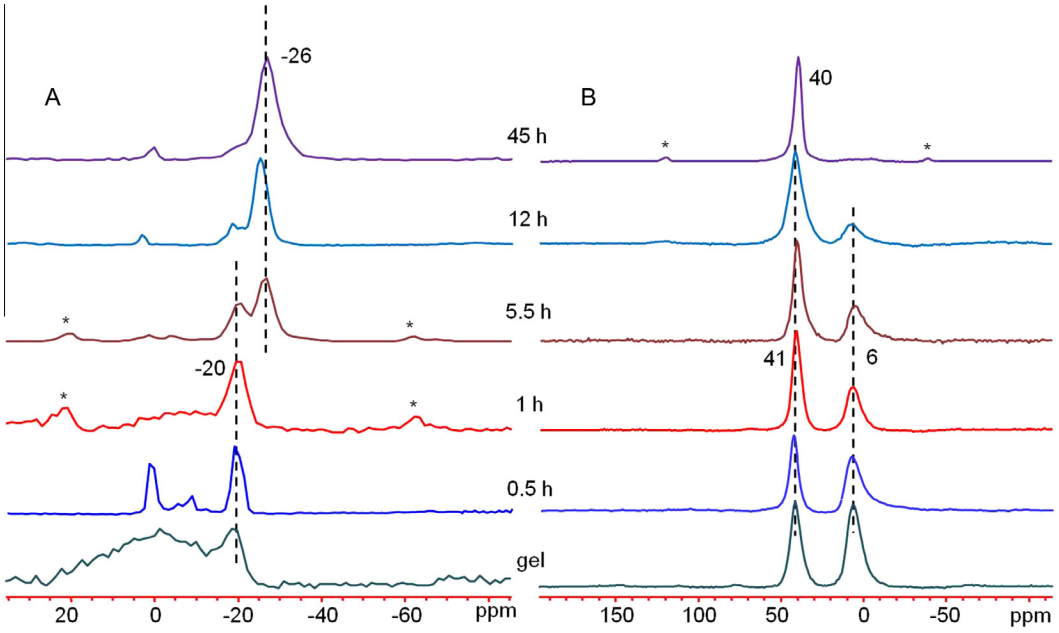

Fig. 9. ^{31}P MAS (A) and ^{27}Al MAS (B) spectra of selected unwashed DGC gel samples. Asterisks indicate spinning sidebands.

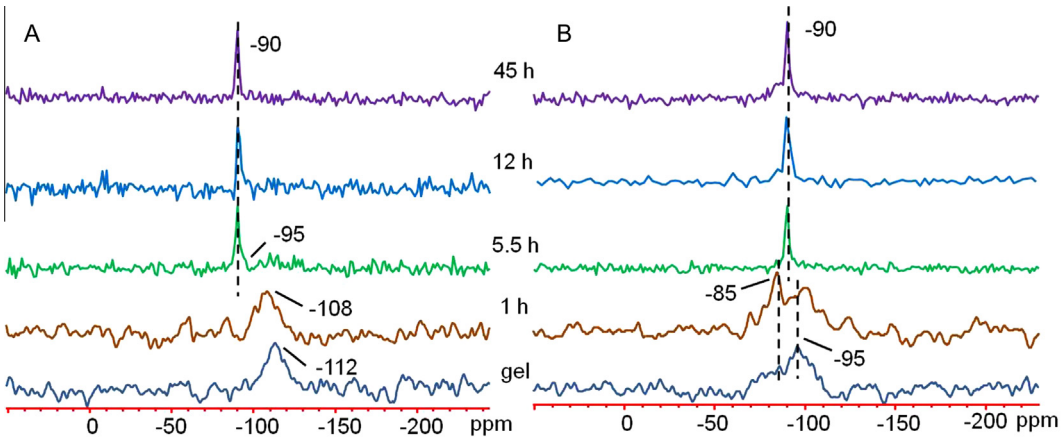

Fig. 10. ^{29}Si MAS (A) and ^{1}H → ^{29}Si CP spectra of selected unwashed DGC gel samples with a contact time of 0.5 ms (B).

broad peaks can be assigned to the unreacted amorphous silica with $Si(OSi)_4$ environments [61]. This indicates that the majority of the silica in the samples heated below 1 h has not reacted and the semi-crystalline phase is mainly AlPO in nature. The CP spectrum of the 1 h sample presents two signals at about −85 and −95 ppm. The −95 ppm peak is due to $(SiO)_2Si(OH)_2$ on the surface of the silica particles [61,62]. The −85 ppm is likely due to the $(AlO)_3SiOH$ or $Si(OAl)_4$ with a SDA nearby in a small amount of amorphous aluminosilicates [61,62]. The results indicate that the silica is activated via formation of aluminosilicate species which are subsequently incorporated into the FAU framework. A similar situation has been reported for SAPO-34 [57]. A sharp peak appears in the ^{29}Si MAS and CP spectra of the 5.5 h sample at around −90 ppm, which is characteristic of isolated $Si(OAl)_4$ species in SAPO-37 [3,33]. The presence of this peak agrees with the corresponding PXRD pattern, ^{31}P and ^{27}Al MAS spectra, which show the existence of SAPO-37 in this sample. ^{29}Si NMR data suggest that the silica first reacts with alumina to form aluminosilicates. The aluminosilicate species then react with the semi-crystalline layered AlPO phase, leading to the Si incorporation and corresponding SAPO-37 formation.

EDX results on selected DGC gel samples are shown in Table 1. A comparison of the Si molar percentages in the two samples synthesized under DGC conditions revealed that Si is gradually incorporated into the framework upon heating the dry gel. The average Si content in 45 h sample is about 13 mol.%, which is the proposed upper threshold value (13%) of SM II mechanism in SAPO-37 framework [46]. Furthermore, the (Si + P)/Al ratio (1.04) is very close to 1, which further supports the SM II mechanism. Therefore, EDX data indicate that under DGC conditions, Si enters into the FAU framework only via substitution for P (SM II), which is consistent with the presence of a single sharp peak at −90 ppm in the ^{29}Si MAS spectrum of the 45 h sample (Fig. 10A). This is similar to the synthesis under HTS conditions, where Si is also incorporated into the framework mainly via SM II.

3.3. SAPO-37 formation pathways

For HTS synthesis, the ^{13}C NMR data indicate that the solids heated for less than 16.5 h at 443 K contain the species having the large cavities corresponding to two supercages. Such species is likely the precursor to final FAU framework and was previously identified existing in the solid phases obtained during SAPO-37 synthesis under very similar conditions [22,23]. ^{13}C NMR data also suggest that this precursor does not have sodalite cages, but likely has 4-membered rings (4Rs) and 6Rs since the existence of 4Rs and 6Rs in the solid phase at the initial stage of crystallization was confirmed by *in situ* and *ex situ* UV Raman studies on the assembly mechanism of zeolite X [63,64]. Further heating leads to the cross-linking of the large pore species, developing of sodalite cages under the influence of TMA^+ and the eventual formation of the FAU framework. Such pathway is illustrated in Scheme 2A.

The AFM findings show that the crystal growth mechanism is "birth and spread" with the nuclei containing at least 7 FAU layers, coalescing with the terraces underneath to form the (1 1 1) faces of SAPO-37 framework. The AFM data also suggest that the hydrothermally synthesized SAPO-37 has rough surfaces that are terminated with 6Rs, D6Rs and incomplete sodalite cages.

While the HTS synthesis is carried out in an extremely complicated system where the crystallization involves solid, liquid, and gaseous phases, the DGC method, on the other hand, is conducted in a relatively simple way with all the reactive species are confined in the solids. Like the HTS initial gel, the initial DGC dry gel also contains the AlPO species having large cavities without long-range ordering. This is not surprising, considering that the initial DGC dry gel is prepared by drying the same initial gel solution. Unlike the HTS initial gel where sodalite cage (which is the secondary building units of the FAU framework) does not exist, the DGC dry gel does contain, at least, quasi-sodalite cages that trap the TMA^+, which are presumably attached to the large pore species. This is consolidated by the finding that the sodalite cage exists in the intermediate phase during the formation of zeolite X [63,65]. In the initial DGC dry gel, the large cavities species with quasi-sodalite cages are disordered in the amorphous material, but they cross-link together to form semi-crystalline layered phase under prolonged heating under DGC conditions. Eventually, each large pore in the layer evolves into two well separated supercages. Meanwhile, silica slowly reacts with alumina, yielding small aluminosilicate particles, which are possibly dispersed between the AlPO layers. As mentioned earlier, the forces holding the layers together are weak nonbonding interactions, which promote bond breaking and reforming in the absence of bulk water and hence facilitate the transformation from the layered phase to SAPO-37. In the last step these layers are reorganized and cross-linked together to form the FAU structure and at the same time Si atoms are incorporated into the framework as isolated $Si(OAl)_4$ species. Scheme 2B is the illustration of this pathway.

4. Conclusions

We have examined the formation of SAPO-37 under both HTS and DGC conditions by using an assortment of techniques including PXRD, SEM, AFM, and solid-state NMR. The results indicate that crystallization pathways for HTS and DGC are similar. Under HTS conditions, the precursor initially is only composed of the large cavities whose size is equivalent to two directly connected supercages.

Increasing the crystallization time leads to the slow formation of sodalite cages that are connected to the cavities. Under DGC conditions, the precursor initially not only contains the large cavities, but also quasi-sodalite cages. Thus, the precursors are almost the same. Further, the precursors are mainly AlPO in nature with little or no Si. The Si incorporation involves forming aluminosilicates first and then incorporating isolated $Si(OAl)_4$ species into the FAU framework. The AFM data suggest that SAPO-37 crystal growth under HTS conditions follows the "birth and spread" mechanism and the (1 1 1) crystal surfaces are terminated by different structural building units.

Acknowledgements

Y.H. thanks the Natural Science and Engineering Research Council of Canada for a Discovery grant and a Discovery Accelerator grant. Funding from Canada Research Chair program and the Canada Foundation for Innovation is also acknowledged. We sincerely thank Prof. X. Sun (UWO) for generously allowing us to use his SEM instrument and Ms. R. Li (UWO) for her kind helps with the SEM and EDX measurements.

Appendix A. Supplementary data

Supplementary data associated with this article can be found, in the online version, at http://dx.doi.org/10.1016/j.micromeso.2013.03.026.

References

[1] B.M. Lok, C.A. Messina, R.L. Patton, R.T. Gajek, T.R. Cannan, E.M. Flanigen, US Patent 4440, 871, 1984.
[2] L. Sierra de Saldarriaga, C. Saldarriaga, M.E. Davis, J. Am. Chem. Soc. 109 (1987) 2686–2691.
[3] A.F. Ojo, J. Dwyer, J. Dewing, K.J. Karim, Faraday Trans. 87 (1991) 2679–2684.
[4] E.M. Flanigen, R.L. Patton, S.T. Wilson, Stud. Surf. Sci. Catal. 37 (1988) 13–27.
[5] B.M. Lok, C.A. Messina, R.L. Patton, R.T. Gajek, T.R. Cannan, E.M. Flanigen, J. Am. Chem. Soc. 106 (1984) 6092–6093.
[6] G. Sastre, D.W. Lewis, C.R.A. Catlow, J. Phys. Chem. 100 (1996) 6722–6730.
[7] L. Maistriau, N. Dumont, J.B. Nagy, Z. Gabelica, G. Derouane, Zeolites 10 (1990) 243–250.
[8] S. Dzwigaj, M. Briend, A. Shikholeslami, M.J. Peltre, D. Barthomeuf, Zeolites 10 (1990) 157–162.
[9] M.J. Peltre, M. Briend, A. Lamy, D. Barthomeuf, F. Taulelle, J. Chem. Soc., Faraday Trans. 86 (1990) 3823–3826.
[10] J.A. Martens, P.J. Grobet, P.A. Jacobs, J. Catal. 126 (1990) 299–305.
[11] B.L. Su, D. Barthomeuf, J. Catal. 139 (1993) 81–92.
[12] G. Fernandes, V. Fernandes, Catal. Today 75 (2002) 233–238.
[13] M.J. Peltre, P.P. Man, M. Briend, M. Derewinski, D. Barthomeuf, Catal. Lett. 16 (1992) 123–128.
[14] M. Briend, M.J. Peltre, A. Lamy, P.P. Man, D. Barthomeuf, J. Catal. 138 (1992) 90–100.
[15] M.J. Franco, J. Perez-Pariente, A. Mifsud, T. Blasco, J. Sanz, Zeolites 12 (1992) 386–394.
[16] A. Corma, V. Fornes, J. Perez-Pariente, J. Chem. Soc. Chem. Commun. 8 (1993) 676–678.
[17] M. Briend, A. Lamy, M.J. Peltre, P.P. Man, D. Barthomeuf, Zeolites 13 (1993) 201–211.
[18] M.E. Davis, Microporous Mater. 7 (1996) 159–160.
[19] T.H. Chen, B.H. Wouters, P.J. Grobet, J. Phys. Chem. B 103 (1999) 6179–6184.
[20] T.H. Chen, B.H. Wouters, P.J. Grobet, Colloids Surf. A 158 (1999) 145–149.
[21] L. Maistriau, N. Dumont, J. Nagy, Z. Gabelica, E. Derouane, Stud. Surf. Sci. Catal. 52 (1989) 209–213.
[22] N. Dumont, T. Ito, J. Nagy, Z. Gabelica, E. Derouane, Stud. Surf. Sci. Catal. 65 (1991) 591–602.
[23] T. Ito, N. Dumont, J. Nagy, Z. Gabelica, E. Derouane, Stud. Surf. Sci. Catal. 60 (1991) 11–20.
[24] W. Xu, J. Dong, J. Li, J. Li, F. Wu, J. Chem. Soc., Chem. Commun. 10 (1990) 755–756.
[25] M.H. Kim, H.X. Li, M.E. Davis, Microporous Mater. 1 (1993) 191–200.
[26] P.R. Hari Prasad Rao, M. Matsukata, Chem. Commun. (1996) 1441–1442.
[27] P.R. Hari Prasad Rao, C. Leon y Leon, K. Ueyama, M. Matsukata, Microporous Mesoporous Mater. 21 (1998) 305–313.
[28] T. Tatsumi, N. Jappar, J. Phys. Chem. B 102 (1998) 7126–7131.
[29] R. Bandyopadhyay, Y. Kubota, N. Sugimoto, Y. Fukushima, Y. Sugi, Microporous Mesoporous Mater. 32 (1999) 81–91.
[30] M. Matsukata, M. Ogura, T. Osaki, P.R. Hari Prasad Rao, M. Nomura, E. Kikuchi, Top. Catal. 9 (1999) 77–92.
[31] T. Gullion, J. Schaefer, J. Magn. Reson. 81 (1989) 196–200.
[32] Y. Huang, B.A. Demko, C.W. Kirby, Chem. Mater. 15 (2003) 2437–2444.
[33] C.A. Fyfe, K.C. Wong-Moon, Y. Huang, H. Grondey, Microporous Mater. 5 (1995) 29–37.
[34] D. Hasha, L. Sierra de Saldarriaga, C. Saldarriaga, P.E. Hathaway, D.F. Cox, M.E. Davis, J. Am. Chem. Soc. 110 (1988) 2127–2135.
[35] D. Zhou, J. Xu, J. Yu, L. Chen, F. Deng, R. Xu, J. Phys. Chem. B 110 (2006) 2131–2137.
[36] C. Blackwell, R. Patton, J. Phys. Chem. 92 (1988) 3965–3970.
[37] Q. Gao, J. Chen, R. Xu, Y. Yue, Chem. Mater. 9 (1997) 457–462.
[38] Z. Yan, B. Chen, Y. Huang, Solid State Nucl. Magn. Reson. 35 (2009) 49–60.
[39] A. Tuel, Y. Ben Taarit, Zeolites 14 (1994) 169–176.
[40] S. Hayashi, K. Suzuki, S. Shin, K. Hayamizu, O. Yamamoto, Chem. Phys. Lett. 113 (1985) 368–371.
[41] G. Liu, P. Tian, J. Li, D. Zhang, F. Zhou, Z. Liu, Microporous Mesoporous Mater. 111 (2008) 143–149.
[42] L. Xu, A. Du, Y. Wei, Y. Wang, Z. Yu, Y. He, X. Zhang, Z. Liu, Microporous Mesoporous Mater. 115 (2008) 332–337.
[43] G. Liu, P. Tian, Y. Zhang, J. Li, L. Xu, S. Meng, Z. Liu, Microporous Mesoporous Mater. 114 (2008) 416–423.
[44] S. Qiu, W. Tian, W. Pang, T. Sun, D. Jiang, Zeolites 11 (1991) 371–375.
[45] M. Derewinski, M.J. Peltre, M. Briend, D. Barthomeuf, P.P. Man, J. Chem. Soc., Faraday Trans. 89 (1993) 1823–1828.
[46] D. Barthomeuf, J. Phys. Chem. 97 (1993) 10092–10096.
[47] M.W. Anderson, Curr. Opin. Solid State Mater. Sci. 5 (2001) 407–415.
[48] S.S. Ono, O. Matsuoka, S. Yamamoto, Microporous Mesoporous Mater. 48 (2001) 103–110.
[49] B. Holme, P. Cubillas, J.H. Cavka, B. Slater, M.W. Anderson, D. Akporiaye, Cryst. Growth Des. 10 (2010) 2824–2828.
[50] P. Cubillas, M.W. Anderson, in: J. Čejka, A. Corma, S. Zones (Eds.), Zeolites and Catalysis: Synthesis, Reactions and Applications, Wiley-VCH, Weinheim, 2010, pp. 1–55.
[51] J.I. Paredes, A. Martinez-Alonso, J.M.D. Tascon, Microporous Mesoporous Mater. 65 (2003) 93–126.
[52] T. Wakihara, A. Sugiyama, T. Okubo, Microporous Mesoporous Mater. 70 (2004) 7–13.
[53] T. Wakihara, T. Okubo, J. Chem. Eng. Jpn. 37 (2004) 669–674.
[54] M.W. Anderson, J.R. Agger, J.T. Thornton, N. Forsyth, Angew. Chem. Int. Ed. 35 (1996) 1210–1213.
[55] P. Cubillas, M.A. Holden, M.W. Anderson, Cryst. Growth Des. 11 (2011) 3163–3173.
[56] R. Singh, J. Doolittle Jr., M.A. George, P.K. Dutta, Langmuir 18 (2002) 8193–8197.
[57] L. Zhang, J. Bates, D. Chen, H.Y. Nie, Y. Huang, J. Phys. Chem. C 115 (2011) 22309–22319.
[58] B. Chen, Y. Huang, J. Phys. Chem. C 111 (2007) 15236–15243.
[59] B. Chen, C.W. Kirby, Y. Huang, J. Phys. Chem. C 113 (2009) 15868–15876.
[60] B. Chen, Y. Huang, Microporous Mesoporous Mater. 143 (2011) 14–21.
[61] G.E. Maciel, C.E. Bronnimann, R.C. Zeigler, I.S. Chuang, D.R. Kinney, E.A. Keiter, Adv. Chem. Ser. 234 (1994) 269.
[62] C. Doremieux-Morin, C. Martin, J.M. Bregeault, J. Fraissard, Appl. Catal. 77 (1991) 149–161.
[63] G. Xiong, Y. Yu, Z. Feng, Q. Xin, F.S. Xiao, C. Li, Microporous Mesoporous Mater. 42 (2001) 317–323.
[64] F. Fan, Z. Feng, G. Li, K. Sun, P. Ying, C. Li, Chem. Eur. J. 14 (2008) 5125–5129.
[65] B. Lok, T. Cannan, C. Messina, Zeolites 3 (1983) 282–291.